

Internal shocks in the jets of radio–loud quasars

Maddalena Spada¹, Gabriele Ghisellini², Davide Lazzati^{2,3} & Annalisa Celotti⁴

¹ *Osservatorio Astrofisico di Arcetri, Largo E. Fermi 5, I-50125 Firenze*

² *Osservatorio Astronomico di Brera, Via Bianchi 46, I-23807 Merate (Lc), Italy*

³ *Present address: Institute of Astronomy, University of Cambridge, Madingley road, Cambridge CB3 0HA, U.K.*

⁴ *S.I.S.S.A., Via Beirut 2/4, I-34014 Trieste, Italy*

E-mail: spada@arcetri.astro.it, gabriele@merate.mi.astro.it, lazzati@ast.cam.ac.uk, celotti@sissa.it

27 October 2018

ABSTRACT

The central engine causing the production of jets in radio sources may work intermittently, accelerating shells of plasma with different mass, energy and velocity. Faster but later shells can then catch up slower earlier ones. In the resulting collisions shocks develop, converting some of the ordered bulk kinetic energy into magnetic field and random energy of the electrons which then radiate. We propose that this *internal shock scenario*, which is the scenario generally thought to explain the observed gamma–ray burst radiation, can work also for radio sources in general, and for blazar in particular. We investigate in detail this idea, simulating the birth, propagation and collision of shells, calculating the spectrum produced in each collision, and summing the locally produced spectra from those regions of the jet which are simultaneously active in the observer’s frame. We can thus construct snapshots of the overall spectral energy distribution as well as time dependent spectra and light curves. This allows us to characterize the predicted variability at any frequency, study correlations among the emission at different frequencies, specify the contribution of each region of the jet to the total emission, find correlations between flares at high energies and the birth of superluminal radio knots and/or radio flares. The model has been applied to qualitatively reproduce the observed properties of 3C 279. Global agreement in terms of both spectra and temporal evolution is found. In a forthcoming work, we explore the constraints which this scenario sets on the initial conditions of the plasma injected in the jet and the shock dissipation for different classes of blazars.

Key words: gamma rays: bursts — X-rays: general — galaxies: active

1 INTRODUCTION

Recent developments in the blazar field, mainly stimulated by the discovery that these sources are strong γ –ray emitters, are offering new and important clues for understanding relativistic jets. All blazar spectral energy distributions (SED) are characterized by two broad emission peaks e.g. (Fossati et al. 1998), strongly variable on different timescales (Wagner & Witzel 1995; Maraschi et al. 1994; Hartman et al. 1996). The location of these peaks (their frequency, relative and absolute flux) and their variability behavior are a strong diagnostic tools to discriminate among theoretical models and find the intrinsic physical parameters of the source. The broad band spectrum from the far infrared upwards can be explained by a “single-zone” model, where the two peaks are respectively due to synchrotron and inverse Compton scattering from the same relativistic electron population (Maraschi, Ghisellini & Celotti 1992; Sikora, Begelman & Rees 1994). Since the radiative cooling time is much

shorter than the dynamical one, the emitting particles must be accelerated *in situ* all along the jet, by means of a process not yet univocally determined.

The high energy flux varies generally on a timescale of the order of a day, and the bulk Lorentz factor (BLF) Γ of the jet is estimated around 10 (Ghisellini et al. 1993), leading to an upper limit for the source dimension of the order of $R \approx 10^{17}$ cm. Furthermore, the required transparency for γ –rays to the process of photon–photon pair production, sets a lower limit in the most powerful sources, of order $\approx 10^{17}$ cm, to the typical distance where the bulk of the radiative dissipation occurs.

Blazars are also characterized by strong radio emission, with a flat spectrum [$F(\nu) \propto \nu^{-\alpha}$, with α between ~ -0.5 and ~ 0.5] and variability time scales of the order of weeks, months (see e.g. Ulrich, Maraschi & Urry, 1997). While the emission at frequencies from the far infrared upwards can be consistently due to a single population of electrons in the inner parts of the jet, the emission in the radio band

has to be generated – in order not to be self-absorbed – on the outer, parsec scales where the plasma properties are expected to be different. The bulk motion is still relativistic at such distances, with BLFs similar to those inferred on the sub–parsec scales, $\Gamma \sim 10$ (Zensus et al. 1997).

The existing models, both homogeneous (e.g. Sikora, Begelman & Rees 1994; Inoue & Takahara 1996) and inhomogeneous ones (e.g. Celotti, Maraschi & Treves 1991; Ghisellini & Maraschi 1989), estimate the jet plasma properties, the magnetic field B and the random Lorentz factors (RLF) of the electrons emitting at the peak of the spectra, γ_p , by fitting the observed SED. In the inner jet $B \approx 1$ G and γ_p varies from $\sim 10^2$ to 10^6 depending on the power of the source (Ghisellini et al. 1998): for the powerful OVV quasars – with bolometric luminosity of the order of $L \approx 10^{47} - 10^{48}$ erg s $^{-1}$ – the synchrotron peak is at infrared-optical frequencies and γ_p is estimated around 10^{2-3} , while for the less powerful sources, like the weak BL Lacs – with $L \approx 10^{44} - 10^{45}$ erg s $^{-1}$ – the synchrotron emission peaks in the UV–X-ray range and the RLFs of the electrons must be higher, $\gamma_p \sim 10^{4-6}$. This trend of decreasing peak energy with increasing source power appears to be systematic and can be accounted for by a corresponding increase in the intensity of a photon field external to the jet, which enhances the inverse Compton cooling losses (Fossati et al. 1998; Ghisellini et al. 1998). In the parsec scale jet the observed (radio) emission is believed to be synchrotron and the corresponding magnetic field and electrons RLF are estimated to be $B \approx 10^{-3}$ G and $\gamma_p \approx 100$, leading to particle cooling timescales much longer than the dynamical one.

Although these studies have allowed us to consistently derive the physical parameters in the emitting region, many aspects in the understanding of relativistic jets remain open, most notably the jet energetics and particle acceleration. In order to explore these issues and their relationship we consider a scenario where the plasma characteristics are not treated as free parameters, but are the result of the jet dynamics, thus relating the observed emission properties to the transport of energy along the jet. We achieve that by *quantitatively* considering a general scenario for the interpretation of blazars analogous to the standard scenario proposed to explain gamma–ray bursts, which was actually originally proposed for blazars more than two decades ago (Rees 1978).

The most important assumption in this scenario is that the central power engine produces energy which is channeled into jets in an intermittent way, though such a time dependent process cannot be easily inferred from first principles.

If the physical conditions determining the energy deposition are not steady, the distribution of BLFs and masses is non-uniform within the ejecta: faster portions of the flow would then catch up with slower ones leading to the development of relativistic shocks. The shocks would plausibly heat the expanding ejecta, generate/amplify a tangled magnetic field and accelerate leptons to relativistic energies, in turn causing synchrotron and inverse Compton emission. In this scenario – named internal shock model (e.g. Rees & Meszaros 1994; Lazzati, Ghisellini & Celotti 1999; Panaitescu, Spada & Meszaros 1999) – the following observational characteristics can be naturally explained:

- **Efficiency** – The radiative output of radio sources in general, and blazars in particular, has to be a small frac-

tion of the energy transported by the jet (less than 10%): extended radio structures require in fact a power input exceeding what is emitted (e.g. Rawlings & Saunders 1991; Celotti & Fabian 1993). Low efficiency is indeed a characteristic of the internal shock model, as the range of the BLFs of the colliding shells can be only small (say the ratio of the maximum and minimum ones $\Gamma_M/\Gamma_m \sim 3$) in order to have a resulting jet bulk motion on larger scale with $\Gamma \approx 10$.

- **Minimum distance for dissipation** – As mentioned in the Introduction, there is a minimum dimension for the γ -ray source and the bulk of the observed power must be produced at some distance from the jet apex, i.e. from the accretion disk. In other words, the emitting zone must be far away from X-rays sources and not extremely compact itself otherwise, quite inevitably, the high energy γ -rays are absorbed by the dense radiation fields. The electron–positron pairs generated by such photon–photon interaction would then re-process the γ -ray power into softer (especially X-ray) radiation, which is not observed (Ghisellini & Madau 1996). In the internal shock model the jet becomes radiative on scales much larger than the central source dimension ($R_0 \approx 10^{14}$ cm for a black hole of $M = 10^9 M_\odot$) since all the velocities are close to c and therefore the shells propagate for a significant distance before collisions can start. The expected minimum distance for the γ -rays emission is of the order of $R \approx R_0 \Gamma^2 \approx 10^{16} - 10^{17}$ cm, where R_0/c measures the time interval between two consecutive shell ejections.

- **Variability** – Clearly the observed large amplitude variability must be explained by a non steady–state model: we believe that the shell–shell collision scenario studied here is the simplest among them.

- **Continuous energy deposition along the jet** – Dissipation is observed to occur along the whole jet, from the inner to the parsec scales with decreasing luminosity and typical photon frequency. The dynamical evolution of a wind in the internal shock model can indeed reproduce such behavior: shell–shell collisions take place along the whole jet, leading to a continuous conversion of bulk energy into internal one over a large range of distances. Due to the averaging of the shell BLFs during the expansion, the collisions become progressively less efficient as the distance increases, thus progressively reducing the released internal energy, the electron RLF, and the magnetic field.

As this scenario allows to predict a general and fairly complete description of the *entire* radiative jet, we believe that it can be a powerful tool to understand blazar spectra, their variability and the possible correlations between observed quantities on different scales. While we plan to fully explore the large potentialities of this model in a forthcoming work, in this paper we present the basic assumptions and the general set up of the model. For illustration purposes (i.e. not aiming to determine precise values of the physical quantities) we also consider the case of a specific well studied blazar, specifically 3C 279. Section 2 therefore describes the dynamics of the wind and the shocks forming from shell collisions, while in Section 3 the radiative properties of the shocked plasma are presented. The numerical simulations for the time dependent evolution of the system are described in Section 4, while the results and the specific case of 3C 279 are the subject of Section 5. In the final Section 6 we discuss our findings.

2 HIERARCHICAL INTERNAL SHOCKS

The entire jet emission is simulated by adding pulses radiated in a series of internal shocks that occur in a unstable relativistic wind (Daigne & Mochkovitch 1998; Spada, Panaitescu & Meszaros 2000). After (parametrically) setting the dynamics of the wind ejection, we calculate the radii where the shells collide. For each collision we study the hydrodynamics, in order to determine the shock velocity, the compression ratio and the internal energy E_{sh} of the shocked fluid. Assuming a given partition of E_{sh} among protons, electrons and magnetic field we calculate the relevant physical parameters in the shocked fluid, and finally the features of the emitted radiation.

2.1 Ejection features

The wind is discretized as a sequence of $N = t_w/t_v$ shells, where t_w is the duration time of the wind ejection from the central source and $t_v \ll t_w$ is the average interval between consecutive ejections. Each shell is characterized by a mass M_j , a bulk Lorentz factor Γ_j and an ejection time t_j : at $t = t_j$ the j -th shell is at a distance $R_j = R_0$, where R_0 is the central source dimension ($R_0 = 10^{14}$ cm).

The shell BLFs Γ_j are chosen randomly from a uniform distribution between Γ_m and Γ_M , and the shell masses are also randomly picked up from a uniform distribution with an average value M_t/N , where the total mass in the wind M_t is determined by the requirement:

$$\sum_{j=1}^N M_j \Gamma_j c^2 = L_w t_w \quad (1)$$

where L_w is the wind luminosity. The time interval between the ejection of a couple of consecutive shells is assumed to mimic a scenario in which the inner engine behaves as an accumulation mechanism: the quiescent time between the ejection of the j^{th} and the $(j+1)^{\text{th}}$ shells is proportional to the total energy in the $(j+1)^{\text{th}}$ shell.

The ejected shell width Δ_j is of the same order of the central source dimension R_0 and the shell internal energy U_j is negligible (all the energy is stored as bulk kinetic energy).

2.2 Wind dynamics

The dynamics of the wind expansion is characterized by a series of two-shell collisions in which the faster shells catch up with the slower ones in the outer parts of the ejecta. The calculation of the collision radii follows the procedure of Kobayashi, Piran & Sari (1998). Given the wind configuration after the i -th collision, i.e. shell radius $R^i(j)$, shell velocity $\beta^i(j)$, shell width $\Delta^i(j)$ and expansion velocity of the shell $\beta_e^i(j)$, we calculate the minimum value among all the collision times between pairs of shells $(j, j-1)$ with $\beta_{j-1} > \beta_j$.

$$\delta t_{i+1} = \min(t_{j,j-1}) \quad (2)$$

$$t_{j,j-1} = \frac{R(j) - R(j-1) - 0.5(\Delta(j) + \Delta(j-1))}{\beta(j-1) - \beta(j) + 0.5(\beta_e(j) + \beta_e(j-1))}. \quad (3)$$

The radius of the $(i+1)$ -th collision represents the position of the two shells colliding after δt_{i+1} . This procedure is iterated

for a wind described by an up-dated configuration, with a merged shell instead of the two colliding ones.

Regarding the two-shell interaction as an inelastic collision, the momentum and energy conservation laws yield the physical properties of the merged shell. If (Γ_i, M_i, η_i) and (Γ_o, M_o, η_o) are the BLFs, rest masses and internal energies of the fast (inner) and slow (outer) shell with $\Gamma_i > \Gamma_o$, the merged shell has a rest mass $M_m = M_i + M_o$, a BLF given by:

$$\Gamma_m = \left(\frac{\mu_i \Gamma_i + \mu_o \Gamma_o}{\mu_i / \Gamma_i + \mu_o / \Gamma_o} \right)^{1/2} \quad (4)$$

where $\mu_i = M_i + \eta_i/c^2$ and $\mu_o = M_o + \eta_o/c^2$. The total internal energy of the merged shell will then be:

$$E_{\text{in}} = \eta_i + \eta_o + \mu_i c^2 (\Gamma_i - \Gamma_m) + \mu_o c^2 (\Gamma_o - \Gamma_m). \quad (5)$$

The dynamical efficiency, namely the newly generated internal energy over the total energy, is given by:

$$\epsilon_d = \frac{\mu_i (\Gamma_i - \Gamma_m) + \mu_o (\Gamma_o - \Gamma_m)}{\Gamma_i \mu_i + \Gamma_o \mu_o}. \quad (6)$$

This efficiency decreases with the ratio Γ_i/Γ_o and is maximized for $\mu_o = \mu_i$.

The width of the shells spreads between two consecutive collisions with a velocity:

$$\beta_e = \frac{2\beta'_s}{\Gamma^2} \frac{1}{1 - (\beta\beta'_s)^2}, \quad (7)$$

as measured in the observer's frame, where $\beta'_s c = v'_s$ is the sound velocity of the plasma in the shell co-moving frame:

$$v'_s = \sqrt{\frac{1}{3} \frac{E'_{\text{th}}}{M_{\text{sh}}}}. \quad (8)$$

During the free expansion between two subsequent collisions, each shell loses internal energy for adiabatic losses, while the BLF is held constant. The magnetic field, on the contrary, is generated at each collision without keeping memory of the field generated in precedent collisions (if any). The plasma thermal energy E_{th} increases in each collision – by the fraction of E_{in} which is not used to either accelerate electrons to a power-law energy distribution and/or generate/amplify magnetic field – leading to an increase in the plasma sound velocity v'_s during the wind expansion.

Since during each collision the propagation of the shocks through the two shells compresses the width of the merged shell Δ_m , the calculation of Δ_m itself requires a hydrodynamic treatment of the interaction, that is presented in the next section.

2.3 Hydrodynamic of the two-shell interaction

Let us consider the dynamics of the interaction between two shells. Here it will be assumed that the presence any magnetic field is negligible from the dynamics point of view. During the collision two shocks are formed, separated by a contact discontinuity: a forward shock (FS) that propagates in the external slow shell and a reverse shock (RS) that propagates backward in the faster shell (see Figure 1).

The calculation of the shocked plasma BLF, Γ_{sh} , in the lab frame can be done applying the following conditions (Panaitescu & Mészáros 1999):

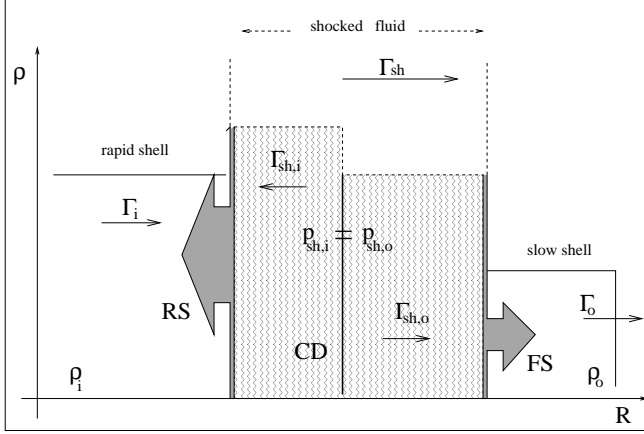


Figure 1. Diagram of a two-shell collision. A inner fast shell with BLF Γ_i and density ρ_i catches up with a slower shell characterized by BLF Γ_o and density ρ_o . The reverse shock (RS), propagating in the inner shell, and the forward shock (FS), propagating in the outer shell, are shown. Both of the shocked fluids move with BLF Γ_{sh} in the lab frame. In the un-shocked fluid frame the RS BLF is $\Gamma_{sh,i}$ and the FS BLF is $\Gamma_{sh,o}$. The co-moving pressures of the shocked fluids are equal around the contact discontinuity, $(p_{sh})_i = (p_{sh})_o$.

- The Blandford–McKee (1976) jump equations for the FS and RS. For the FS the energy and particle number conservation yield:

$$\left(\frac{e_{sh}}{n_{sh}}\right)_o = m_p c^2 (\Gamma_{sh,o} - 1) \quad (9)$$

$$\left(\frac{n_{sh}}{n}\right)_o = \frac{\hat{\gamma} \Gamma_{sh,o} + 1}{\hat{\gamma} - 1}, \quad (10)$$

where e_{sh} and n_{sh} are the internal energy and the numerical baryon density of the shocked plasma, respectively, and n is the pre-shocked numerical density. All these quantities are measured in the fluid co-moving frame. $\hat{\gamma}$ is the adiabatic index and $\Gamma_{sh,o}$ is the BLF of the shocked plasma in the frame of the outer shell. A similar set of equations holds for the RS. The shocked plasma pressure $p = (\hat{\gamma} - 1)u$ is calculated through Eqs. (9) and (10): $(p_{sh})_{o(i)} = (\Gamma_{sh,o(i)} - 1)(\hat{\gamma} \Gamma_{sh,o(i)} + 1) \rho_{o(i)} c^2$, with $\rho_{o(i)}$ being the co-moving matter density of the shells before the collision.

- The condition of equal pressure for the shocked fluids around the contact discontinuity (CD) $(p_{sh})_o = (p_{sh})_i$, and the condition of equal velocity around the CD yield a quartic equation for the lab-frame BLF Γ_{sh} :

$$\hat{\gamma}(g^4 - Y)x^4 + 2(\hat{\gamma} - 1)g(Y - g^2)x^3 + 2(2 - \hat{\gamma})g^2(Y - 1)x^2 + 2(\hat{\gamma} - 1)g(g^2Y - 1)x + \hat{\gamma}(1 - g^4Y) = 0, \quad (11)$$

where:

$$x = \frac{\Gamma_{sh}}{\sqrt{\Gamma_o \Gamma_i}}, \quad g = \sqrt{\frac{\Gamma_i}{\Gamma_o}} \quad \left(\frac{1}{g} < x < g\right), \quad (12)$$

where Γ_o and Γ_i are the initial BLFs of the two shells and Y is the ratio of the pre-shocks densities of the slow and fast shells. Eq.(11) is solved numerically. In the range of interest and for any physical choice of parameters Eq.(11) yields only one solution.

Once Γ_{sh} is known we can evaluate:

- The shell widths after the shocks. The compression ratio ρ/ρ_{sh} is obtained by the jump conditions (9) and (10) (assuming a value for the adiabatic index $\hat{\gamma} = 4/3$) and:

$$\Delta_{sh,i} = \Delta_i \left(\frac{\rho_i}{\rho_{sh,i}}\right)_{lab} \quad \Delta_{sh,o} = \Delta_o \left(\frac{\rho_o}{\rho_{sh,o}}\right)_{lab}, \quad (13)$$

where Δ_i and Δ_o are the pre-shock values.

- The internal energies E_{RS} and E_{FS} for the RS and FS. The equality of the two shocks velocities and of the comoving internal energy densities yields (in the lab frame) to:

$$\frac{E_{RS}}{E_{FS}} = \frac{\Delta_{sh,i}}{\Delta_{sh,o}} = R. \quad (14)$$

Thus the energy in the RS is $E_{RS} = R/(1 + R) \times E_{in}$, and in the FS is $E_{FS} = 1/(1 + R) \times E_{in}$, where E_{in} is the total internal energy generated during the collision (eq. 5).

- Knowing the shell width and the shock velocity we can then estimate the shell crossing time of the shock $\delta t_{cr} = \Delta/|v_{sh} - v_0|$ where v_{sh} and v_0 are the post-shock and pre-shock material velocity, respectively.

2.4 Shocked fluid parameters

The parameters determining the synchrotron and inverse Compton emission are the magnetic field strength B and the electron energy distribution in the shocked fluid.

Given the uncertainty in determining these quantities directly from the physics of relativistic shocks, these are parametrized by dimensionless parameters defined as: ϵ_B and ϵ_e , which measure the fraction of the co-moving internal energy density U'_{sh} stored in magnetic field U'_B and in electrons U'_e , respectively (the apex indicates quantities measured in the co-moving frame).

The co-moving magnetic field is then defined by $B'^2/(8\pi) = \epsilon_B U'_{sh}$:

$$B' = \frac{1}{\Gamma_{sh}} \sqrt{\frac{2\epsilon_B E_{sh}}{R^2 \Delta}}, \quad (15)$$

and is assumed to be randomly oriented in space.

Following the results on non-relativistic shocks, and the recent results on relativistic ones (Bednarz & Ostrowski 1998; Kirk et al. 2000), we also postulate that the electrons are accelerated (instantaneously) behind the shock as a power law $N(\gamma) \propto \gamma^{-p}$ with $\gamma > \gamma_b$, and $p > 2$. For an equal number of protons and electrons, the number density of non-thermal electrons is: $n'_e = \zeta_e \rho_{sh}/m_p$, where ζ_e is the fraction of electrons effectively accelerated. Since $U'_e = \epsilon_e U_{sh}$, the minimum RLF γ_b corresponds to:

$$\gamma_b = \frac{p-2}{p-1} \left(1 + \frac{\epsilon_e U'_{sh} m_p}{\zeta_e \rho'_{sh} m_e}\right) \approx 1837 \frac{p-2}{p-1} \frac{\epsilon_e}{\zeta_e} \Gamma_{sh}. \quad (16)$$

In conclusion, by studying the wind dynamics and shock hydrodynamics we can determine for each collision the energy density in non-thermal electrons and in magnetic field and estimate the minimum RLFs γ_b of the electron energy distribution injected by the shocks.

3 THE SPECTRUM

Having estimated such quantities, we can therefore calculate the spectrum of the radiation emitted during each collision. In order to achieve that we adopt some simplifications:

- The emitting zone is assumed to be homogeneous, and the plasma is embedded in a tangled magnetic field. Its co-moving volume is $V = \pi\psi^2 R^2 \Delta R'$, where ψ is the half-opening angle of the jet, assumed conical.

- The relativistic particles are treated as having the same energy distribution throughout the entire emitting region. In a more realistic approach, the particles would be accelerated at the shock front, where most of the energetic electrons would be located, while cooled particles would be progressively more distant from the shock front. However, as we are interested in the “average” spectrum, we assume to collect radiation emitted by the entire shell. Clearly such simplification does not allow to consider changes in spectral details occurring on a timescale faster than the light crossing time of a single shell.

- There is a source of soft photons external to the jet. We identify it with the emission reprocessed in the broad line region (BLR). Therefore we consider a luminosity $L_{\text{ext}} = aL_{\text{disk}}$ is produced within R_{BLR} , corresponding to a radiation energy density (as measured in the frame comoving with the shell) given by (e.g. Ghisellini & Madau 1996):

$$U_{\text{ext}} = \frac{17}{12} \frac{aL_{\text{disk}}\Gamma^2}{4\pi R_{\text{BLR}}^2 c} \quad (17)$$

For simplicity, this seed photon component is considered to abruptly vanish beyond R_{BLR} .

- We assume that the particle distribution results from the continuous injection and cooling processes, where particles are injected with a power law energy distribution of index $s = (p - 1)$ between γ_b and γ_{max} (as measured in the comoving frame). The corresponding power injected in the form of relativistic particles is L_e . The equilibrium particle distribution $N(\gamma)$ is then found through the following procedure.

We calculate the (comoving) random RLF γ_{cool} of those particles with a cooling time comparable with the shock crossing time t_{cross} and above γ_{cool} the distribution is taken as a power law of index p . Below γ_{cool} there are two cases:

- if $\gamma_{\text{cool}} > \gamma_b$, we assume that $N(\gamma) \propto \gamma^{-s}$ between γ_b and γ_{cool} , and $N(\gamma) = 0$ for $\gamma < \gamma_b$;
- if $\gamma_{\text{cool}} < \gamma_b$, $N(\gamma) \propto \gamma^{-2}$ between γ_{cool} and γ_b , and $N(\gamma) = 0$ for $\gamma < \gamma_{\text{cool}}$.

The normalization of $N(\gamma)$ is determined according to whether particles with $\gamma \sim \gamma_b$ can or cannot cool in the timescale t_{cross} :

- if most of the power injected in relativistic particles is radiated in a short timescale ($< t_{\text{cross}}$, this is equivalent to demand $\gamma_b > \gamma_{\text{cool}}$) we apply a luminosity balance condition:

$$L_e = V m_e c^2 \int \dot{\gamma} N(\gamma) d\gamma, \quad (18)$$

where V is the emitting volume and $\dot{\gamma}$ is the total radiative cooling rate, which includes synchrotron, synchrotron self-Compton (SSC) and external Compton (EC) losses. In order to allow for the possibility of having multiple Compton scatterings, especially when γ_b is not very large, we first calculate how many scattering orders n_{IC} can take place be-

fore the Klein–Nishina limit is reached (we consider up to 10 orders of scatterings). Taking γ_b as the relevant energy, the number of scattering orders in the Thomson regime are

$$n_{\text{IC}} = \frac{\ln(\gamma_b/x_B)}{\ln(4\gamma_b^2/3)} - 1 \quad (19)$$

where $x_B \equiv h\nu_B/(m_e c^2)$ and $\nu_B = eB/(2\pi m_e c)$ is the (non-relativistic) Larmor frequency. We define $U_e \equiv L_e/(\pi R^2 c)$ and introduce the Comptonization parameter y as:

$$y \equiv \frac{3}{4} \sigma_T \Delta R' \int \gamma^2 N(\gamma) d\gamma. \quad (20)$$

Here $\Delta R'$ is the thickness of the shell at the time of the collision. For simplicity, we neglect its further expansion while it is radiating. With this definition of y , Eq. (18) can be re-written as:

$$U_e = y U_B \left(1 + \frac{U_{\text{ext}}}{U_B} + y + y^2 + \dots y^{n_{\text{IC}}} \right). \quad (21)$$

- if most of the power is not radiated in t_{cross} , the electrons retain their energy and

$$E_e = L_e t_{\text{cross}} = m_e c^2 V \int N(\gamma) \gamma d\gamma. \quad (22)$$

Assuming the same broken power-law shape for $N(\gamma)$ we can then determine its normalization.

3.1 Synchrotron emission

To calculate the synchrotron emission we adopt the pitch angle averaged synchrotron emissivity for a single electron given in, e.g., Ghisellini & Svensson (1991):

$$j(\gamma, \nu) = \frac{3\sqrt{3}}{\pi} \frac{\sigma_T c U_B}{\nu_B} t^2 \times \left\{ K_{4/3}(t) K_{1/3}(t) - \frac{3t}{5} [K_{4/3}^2(t) - K_{1/3}^2(t)] \right\}. \quad (23)$$

Here $t \equiv \nu/(3\gamma^2 \nu_B)$ and K_b is the modified Bessel function of order b . The total monochromatic synchrotron luminosity (in the comoving frame) is then found by integrating $j(\gamma, \nu)$ over the particle distribution and the source volume.

3.2 Synchrotron self-absorption

The synchrotron self absorption spectrum produced by a power law energy distribution with a low energy cut-off is $F(\nu) \propto \nu^2$ instead of the familiar $\nu^{5/2}$. The type of distribution can result from the injection of particles above some minimum energy and slow cooling (with respect to t_{cross}). This case is therefore relevant to us. Here we treat synchrotron self-absorption exactly, making use of the concept of “synchrotron cross section” $\sigma_s(\gamma, \nu)$ given in Eq. (2.17) of Ghisellini & Svensson (1991), which we report for completeness:

$$\sigma_s(\gamma, \nu) = \frac{8\sqrt{3}\pi^2}{15} \frac{e}{B} \frac{t}{\gamma^5} [K_{4/3}^2(t) - K_{1/3}^2(t)], \quad (24)$$

where e is the electron charge and a tangled magnetic field and an isotropic distribution of pitch angles are assumed. The synchrotron absorption optical depth is then given by

$$\tau_\nu^s = \Delta R' \int \sigma_s(\gamma, \nu) N(\gamma) d\gamma. \quad (25)$$

Note that in this formalism the optical depth can be determined also when $N(\gamma)$ has abrupt cut-offs.

The resulting monochromatic synchrotron luminosity is isotropic in the comoving frame and is calculated according to the usual radiation transfer equation:

$$L_s(\nu) = 4\pi V \left[\int j(\gamma, \nu) N(\gamma) d\gamma \right] \frac{1 - e^{-\tau_\nu^s}}{\tau_\nu^s}. \quad (26)$$

3.3 Inverse Compton emission

We calculate the inverse Compton emission if it occurs in the Thomson regime, while neglect the Klein–Nishina regime by adopting a scattering cross section equal to the Thomson one for $\gamma x < 3/4$ and zero otherwise. $x = h\nu/(m_e c^2)$ is the dimensionless energy of the incoming photon. The δ -function approximation for the single particle spectrum is adopted, i.e. it is assumed that the particle emission is peaked at $x_c = (4/3)\gamma^2 x$. With these simplifications the resulting emitted monochromatic power is

$$L_c(x_c) = \frac{\sigma_T c V m_e c^2}{2} \int N(\gamma) \gamma n(x) dx; \quad \gamma = \left(\frac{3x_c}{4x} \right)^{1/2} \quad (27)$$

where $n(x)$ is the density of seed photons. Eq. (27) is calculated for each order of Compton scattering. To calculate $L_{c,n}(x_c)$ of the Compton order n we must then use the photon density produced by the previous order, $n(x)_{n-1}$. For the first order, the seed photons are the sum of the locally produced synchrotron and the externally produced photons. The spectrum of the external seed photons (in the comoving frame) is assumed to have a blackbody shape peaking at frequency $x_0 = \Gamma x_{\text{line}}$, where we always assume $\nu_{\text{line}} = 10^{15}$ Hz.

As high energy γ -rays can interact with softer photons producing electron–positron pairs, we take into account the absorption effects due to this process. However in general this is found to be unimportant because no large compactnesses are involved.

3.4 Beaming

Finally let us consider the effect of relativistic beaming on the observed radiation. The emitting plasma is moving at a BLF Γ , intermediate between the original BLF of the two colliding shells, computed according to the details given in Section 2. The radiation produced by each colliding shell is then received by the observer as

$$L^{\text{obs}}(\nu^{\text{obs}}) = \delta^3 L(\nu^{\text{obs}}/\delta), \quad (28)$$

where $\delta = [\Gamma - (\Gamma^2 - 1)^{1/2} \cos \theta]^{-1}$ is the Doppler (or beaming) factor and θ is the viewing angle (with respect to the jet axis). The luminosity thus calculated corresponds to what the observer would estimate assuming isotropic emission.

4 NUMERICAL SIMULATIONS

In this section we analyze the general properties of the macro- and micro-physics of the plasma during the jet evolution. Numerical simulations are mandatory in order to test

the model, given the difficulty in understanding and disentangle the effect of each parameter on the global properties of the flow and the produced radiation.

The number of parameters that sets the kinematical and radiative evolution of the jet flow is relatively small. More precisely, the range of BLFs ($\Gamma_m \div \Gamma_M$), the average kinetic luminosity of the inner engine L_w and the time variability timescale t_v define the kinematical evolution, while the equipartition parameters ϵ_e and ϵ_B and the fraction of accelerated electrons ζ_e control the radiative properties of the plasma. The former ones are reasonably constrained, since $10 \lesssim \Gamma \lesssim 25$ and $L_w \sim 10^{48}$ erg s $^{-1}$ are observationally inferred and the variability time can be estimated as $t_v \sim R_0/c \sim 10^4$ s. On the other hand, it is more difficult to quantify the latter ones and they can be basically considered as free parameters. In the simulations presented in this paper, they have been specifically adjusted in order to reproduce the general observed behavior of the OVV source 3C 279, as: $\epsilon_e = 0.5$, $\epsilon_B = 0.004$ and $\zeta_e = 0.04$.

Finally, the external radiation field (see above) is constrained by the radius of the BLR, $R_{\text{BLR}} = 5 \times 10^{17}$ cm, and by the luminosity of the disk and corona radiative components assumed to be $L = 10^{45}$ erg s $^{-1}$.

In order to illustrate the difficulty in predicting the results of changes in the above parameters, let us consider, as an example, the effect of variations (decrease) in the lower BLF Γ_m . On one side as the average speed of the shells is smaller, they must be more massive to maintain the same wind luminosity. This implies that the energy per baryon generated in each collision is lower and thus a smaller γ_b is expected. On the contrary, the dynamical efficiency increases thanks to the larger ratios of the BLFs of the involved shells, leading in turn to larger internal energy, in direct competition with the former effect. Moreover, a smaller Γ_m causes the collisions to start earlier, when the shell volume is smaller, with the consequent creation/amplification of a larger magnetic field. In summary, even a limited change in a single parameter causes several (often competing) effects in the kinematical and radiative evolution of the flow. Therefore in the following we will examine such consequences through numerical simulations of the flow evolution.

4.1 Output parameters

A first key quantity calculated through the simulations is the distribution of collision radii: this in fact controls the average value of the magnetic field strength (which depends on the shell volume, i.e. on the shock distance), and the number of collisions occurring inside the BLR, which in turns determines the relative importance of the radio-optical to γ -ray flux.

Figure 2 shows the distribution of radii at which collisions take place. The limit at small distances directly follows from the choice of the injection parameters, and its typical value can be approximated as:

$$R_{\text{min}} \approx \frac{2\alpha_\Gamma^2}{(\alpha_\Gamma^2 - 1)} \Gamma_m^2 c t_v \sim 7 \times 10^{16} \text{ cm}, \quad \alpha_\Gamma = \frac{\Gamma_M}{\Gamma_m} \quad (29)$$

for an average time between two ejections $t_v = 10^4$ s, $\Gamma_M = 25$ and $\Gamma_m = 10$. The merged shells collide again and again at larger distances up to $\sim 10^{20}$ cm, where the differences

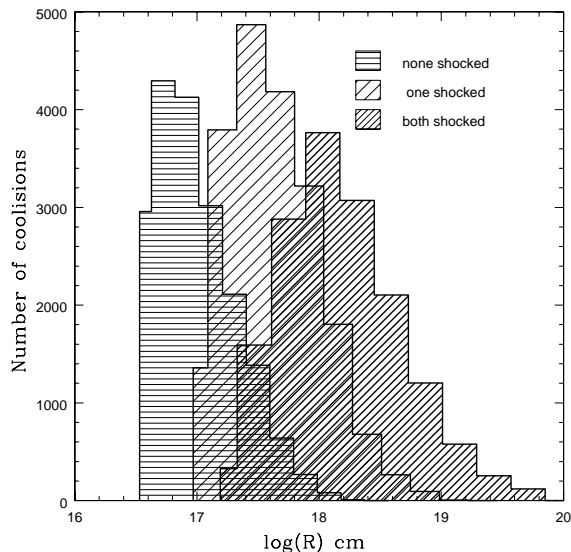


Figure 2. The histograms show the distributions of radii of the collisions between shells that have: never collided before (i.e. with no internal energy), only one has collided before, both have collided before.

among the shell velocities are completely smoothed out and the wind can be considered uniform.

The overall duration of the simulation ($t_w = 10^8$ s, corresponding to 3×10^4 shells) has been chosen in order to reach a virtually steady state for the wind, i.e. with collisions taking place at all radii smaller than $\sim 10^{20}$ cm. As shown in Fig. 2, in the inner part ($R < 10^{18}$ cm) the collisions are mostly between shells which have never collided before, while shells colliding at larger radii (10^{18} – 10^{19} cm) are the result of previous mergings. About 50 per cent of the shocks occur inside the BLR (for $R_{\text{BLR}} = 5 \times 10^{17}$ cm), while only 7.2 per cent take place at radii $R > 10^{19}$ cm.

The net amount of internal energy E_{in} released in each interaction depends on the dynamical efficiency and on the total kinetic energy of the shells available before the collision. As illustrated in the upper panel of Figure 3 the shell BLFs tend to average out during the wind expansion, leading to a strong attenuation of the dynamical efficiency: this can be as high as 10 per cent for the inner collisions but decreases to less than 0.1 per cent at the largest radii. However, the outer shocks involve larger kinetic energies, as the shells are much more massive – being the result of many previous collisions. As a consequence, the average net amount of internal energy generated by each interaction is roughly constant with radius, although as few shells are left in the large scale wind, their rate of collisions is low.

As discussed in the previous section, the internal energy E_{in} is shared among protons, electrons and magnetic field. The central panel of Fig. 3 shows the value of the minimum RLF of the accelerated electrons, γ_b , while the lower panel of Fig. 3 represents the magnetic field strength B for the same collisions. In some cases, the efficiency of the collision is so small that the minimum Lorentz factor of the accelerated electrons is lower than 2. Also the magnetic field is usually small in these cases. These collisions are not considered in

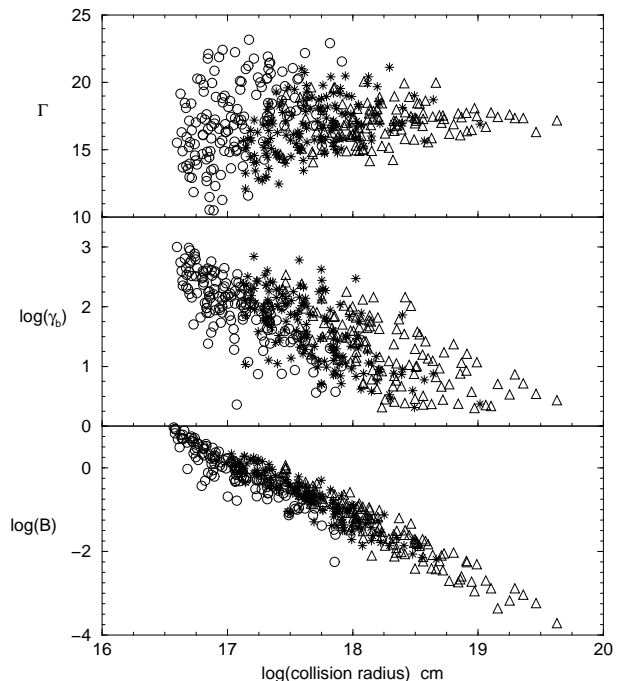


Figure 3. Evolution of the post-shock shell parameters as a function of the collision radius. The upper panel shows the BLF of the merged shell after each collision; the central panel represents the minimum RLF of the electrons γ_b (for $\epsilon_e = 0.5$; $\zeta_e = 0.04$); the lower panel shows the value of the generated magnetic field ($\epsilon_B = 0.004$). FS and RS are considered independently. Only one tenth of the points is displayed for clarity. Circles refer to collisions in which none of the shells has ever collided before, pluses to collisions in which one of the shells has collided, while triangles indicate collisions between shells that have both collided before.

the radiative part of the code, since the cooling time of the electrons is so long that adiabatic losses are overwhelming. In any case, the minimum Lorentz factor of the electrons always exceeds the thermal motion of the fraction of non accelerated ones. Since E_{in} is approximately constant with radius, the value of B strongly anti-correlates with the collision distance approximately as $B \propto R^{-1.5}$, being inversely proportional to the square root of the volume.

We can calculate what fraction of the energy produced at each location of the jet is used to accelerate electrons to relativistic energy. In the absence of non-radiative losses, this energy will be eventually entirely radiated. We then call this quantity, which is independent of the specific radiation mechanism and the timescales involved, the “differential radiative efficiency”. The logarithmic differential efficiency, i.e. the efficiency per unit logarithmic radius, is shown in Fig. 4, where we can see that the most radiatively efficient region is the inner jet (between $10^{16.5}$ and 10^{18} cm), where the collision rate is the highest.

The corresponding integrated efficiency, i.e. the fraction of L_w radiated from the beginning of the jet up to a given radius, is shown in Fig. 4: it saturates at $R \sim 10^{19}$ cm at a value of ~ 6 per cent. Such value can in principle depend on the input parameters, but an efficiency of a few per cent is a robust result unless a very broad distribution of the initial BLFs is involved (Beloborodov 2000). Note that the finite duration of the computation does not affect the efficiency

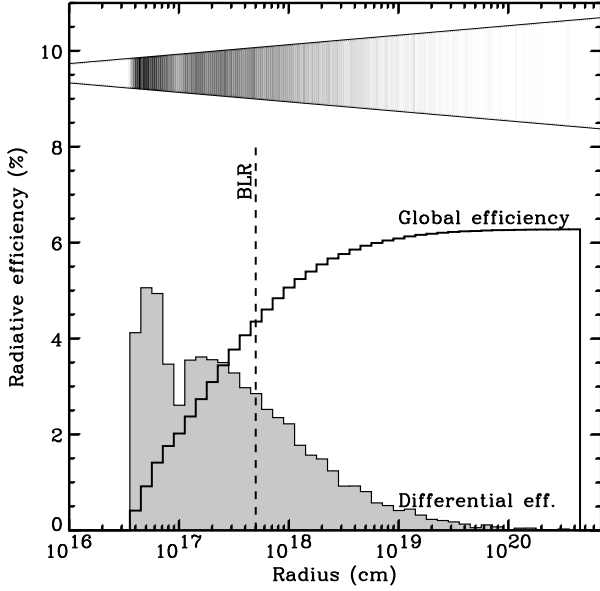


Figure 4. The radiative efficiency versus the collision radius. The solid line refers to the global efficiency, i.e. the fraction of the total kinetic energy of the wind ($E_w = L_w \times t_w$) radiated on scales smaller than a given radius; the shaded histogram shows instead the differential efficiency, namely the fraction of E_w radiated for a given radius interval. The histogram amplitude has been multiplied by a factor of 10 for clarity. The vertical line indicates the radius assumed for the extension of the BLR. The cone-like insert in the upper part of the figure shows a grey-tone representation of the differential efficiency of the jet. The darker the color the higher the efficiency (cfr. the shaded histogram).

estimate, since the differential value approaches zero at radii $\sim 10^{19}$ cm, much smaller than the maximum radius reached in the simulation.

From the micro-physical properties of the plasma shown in Fig. 3 it is also possible to compute the typical frequencies of the emitted photons. For the inner collisions ($R < R_{\text{BLR}}$) synchrotron, SSC and EC are responsible for the observed radiation. At larger radii, external to the photon bath provided by the BLR re-processing, the first two mechanisms dominate the emission. The evolution of the peak frequencies corresponding to the three radiative processes along the jet is shown in Fig. 5, where their values at each radius have been obtained by averaging over all of the collisions occurring at that radius. The synchrotron peak frequency $\nu_{\text{syn}} \propto \gamma_b^2 B$ decreases from $\sim 10^{15}$ Hz for the initial collisions to ~ 1 GHz at pc scale. The SSC peak frequency, given by $\nu_{\text{SSC}} \propto \gamma_b^2 \nu_{\text{syn}}$, varies from $\sim 10^{20}$ to $\sim 10^{16}$ Hz, for R increasing from 3×10^{16} to 10^{18} cm. Finally the EC typical frequency $\nu_{\text{EC}} \approx \Gamma_m^2 \nu_b^2 \nu_{\text{line}} \approx 10^{23}$ Hz (for $\nu_{\text{line}} = 10^{15}$ Hz).

Let us now consider the evolution of the effective radiative efficiency, which is estimated by comparing the radiative time scales δt_γ of relativistic electrons (corresponding to the cooling due to the three above processes) with the time a shock takes to cross the shell width (i.e. the energy injection time) δt_{cr} , and the angular spread time, δt_θ (see Fig. 6). δt_{cr} increases from a few hr at 5×10^{16} cm to \sim a week at 10^{18} cm, because of both the increase in the shell width and the slowing down of the shock velocity during the expansion. The angular spread time reflects the different distances trav-

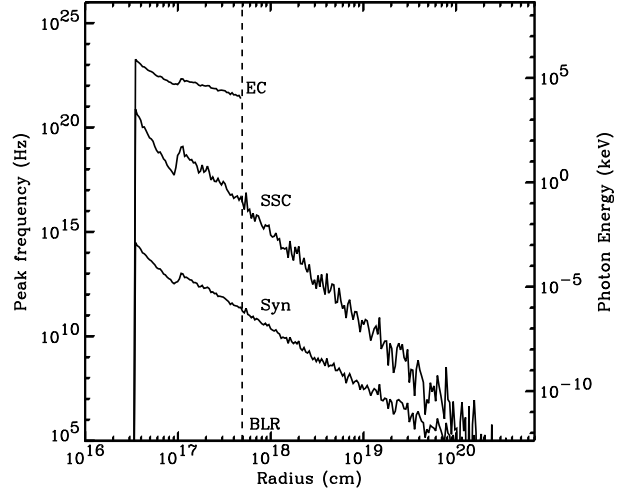


Figure 5. Evolution of the peak frequency of radiation pulses following collisions occurring at different radii, for synchrotron (bottom line), SSC (median line), and EC (upper line).

eled by photons propagating along different directions. Since the observed radiation is beamed in a solid angle $\sim 1/\Gamma$, δt_θ corresponds to the delay in the arrival time of photons emitted at an angle $1/\Gamma$ with respect to those propagating along the line of sight: $\delta t_\theta \approx R/2c\Gamma^2$. This varies from a few hr to \sim a week, analogously to the shell crossing time-scale. The cooling time δt_γ is determined by the most efficient process among synchrotron, SSC and EC. Inside the BLR the latter dominates, with a cooling time of less than a hr, over the ~ 1 day time scale of synchrotron and SSC emission. Outside the BLR, the synchrotron process dominates the emission, with strongly radial dependent cooling times $t_{\text{syn}} \approx 1$ yr*. Note that inside the BLR the cooling is so efficient that electrons emit most of their energy immediately after being accelerated and the pulse duration is due to a combination of the shock crossing time and geometrical effects. At these radii, the radiation is mostly emitted (via EC) at high frequencies, $\sim 10^{22} - 10^{24}$ Hz. Outside the BLR instead electrons cool on a time scale much longer than δt_{cr} , and thus the pulse duration is set by the synchrotron cooling time and the peak frequency is in the mm range.

5 RESULTS

Via the numerical simulations the full time-resolved spectral behavior of the source can be determined. In this section, we directly perform comparisons of the model output quantities with observational data relative to 3C 279, by decomposing the information into (snapshots or time averaged) spectra and light curves. The full time-dependent behavior of the simulated source can be also examined through animations (see <http://www.merate.mi.astro.it/~lazzati/3C279/>) in which the temporal and spectral evolutions are simultaneously shown.

* Clearly the synchrotron and SSC cooling times increase with radius, since γ_b and B decrease during the expansion.

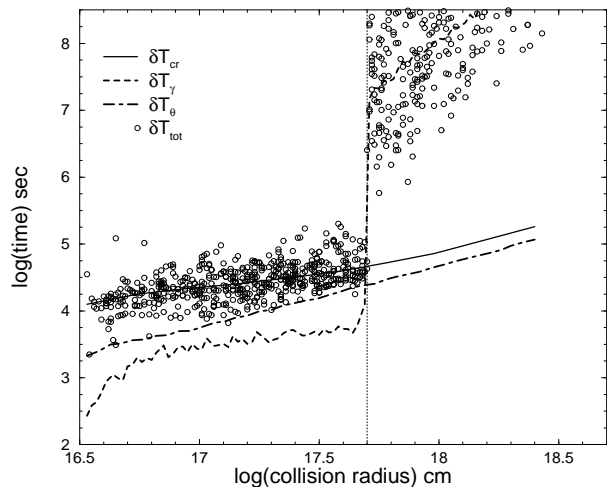


Figure 6. Time scales determining the duration of the observed pulses versus the collision radius. The dashed line refers to the angular spread time, the solid line to the time a shock takes to cross the shells, and the dotted line to the electron cooling time. The circles represent the pulse duration (for clarity we plot only one tenth of the efficient collisions).

The first step of the simulations (see the previous section) determines a set of physical parameters for every collision. In a second step these are then used to produce the Spectral Energy Distributions (SED) emitted in each collision (one SED for the forward and an independent SED for the reverse shock) as described in Section 3. Different spectra are generated in different collisions, but general behaviors which describe the overall shape of the SED as a function of radius can be found. As already stressed the most important condition that affects the SED shape is whether the collision occurs inside or outside the BLR. In Figure 7 we show the averaged spectra of collisions taking place within a given range of radii. Shocks inside the BLR produce spectra dominated by the EC process, through the scattering of electrons with energy $\gamma_b m_e c^2$ on BLR photons. The synchrotron peak, due to the same electrons, is located in the near infrared. A minimum occurs in the optical–UV range, while the X–ray band is characterized by a power–law spectrum. Outside the BLR (lacking the EC component) the SED becomes more and more dominated by the synchrotron process: immediately outside the BLR the Compton parameter $y \sim$ unity and the spectrum is the sum of the synchrotron and the first two Compton orders; as the radius increases, both the relativistic particle density and their average (squared) energy decrease, leading to progressively smaller values of y (if only radiative losses are considered). At the same time the synchrotron self–absorption frequency decreases with radius.

5.1 The observed spectrum

We have so far examined the role of the various emission mechanisms at different distances along the jet. The observed spectrum is the convolution of the emission of all photons arriving at the observer simultaneously: since these are produced at different distances, it is necessary to take into account the different light propagations times when summing them up. In other words, the resulting spectrum is the

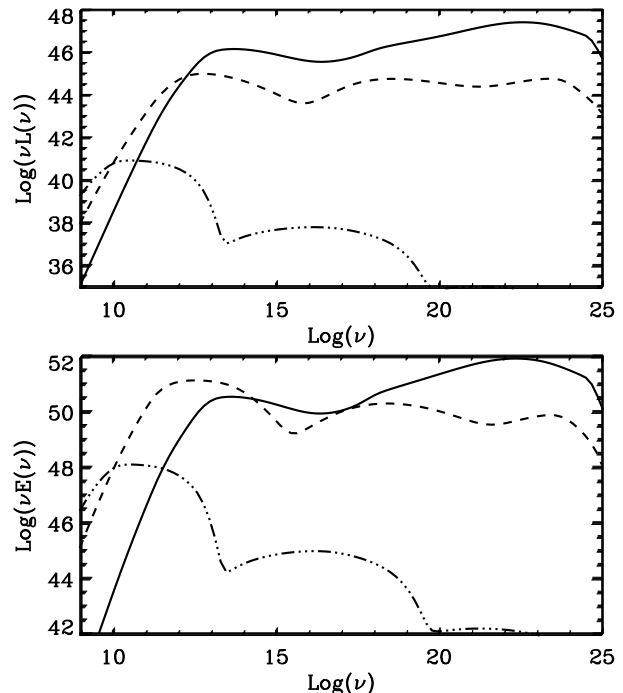


Figure 7. Average spectra of collisions. Solid line show averages for collisions happening inside the broad line region $R < 5 \times 10^{17}$ cm, dashed line shows collisions happening at intermediate distances $5 \times 10^{17} < R < 10^{19}$ cm and dot–dashed line show collisions at large radii ($R > 10^{19}$ cm). Upper panel show the average spectrum of the shells without taking into account the duration of the emission. The Figure show the average spectrum of a single shell in the given range of radii. In the lower panel, instead, the duration of the emission of each collision has been taken into account. The plot shows the average instant spectrum of the whole section of the jet.

sum of all the spectra produced by shocks simultaneously active in the observer frame, taking into account the radius at which each collision is occurring and the travel path of photons to reach the observer.

We therefore associate to each spectrum a photon pulse, with a start time (the time at which the collision begins) and a duration (set by the combination of the timescales discussed in Section 4). The shape of such pulse is triangular if its duration is determined by geometrical effects and/or by the shock crossing time (with a FWHM equal to the timescale shown in Fig. 6): these are generally associated to collisions inside the BLR. If the pulse duration is instead set by cooling the pulse rises linearly, as in the previous case, but after the maximum it decays exponentially [$\propto \exp(-t/3t_{\text{cool}}(\gamma_b))$]: in this case the rise and decay times can be very different.

5.2 The spectrum of 3C 279

Examples of the resulting spectra are compared to data from three different simultaneous multiwavelength campaigns of 3C279 in Figure 8. Note the remarkable variability, especially at γ –ray energies.

Within the model examined here the source high state corresponds to a time interval in which at least one of the

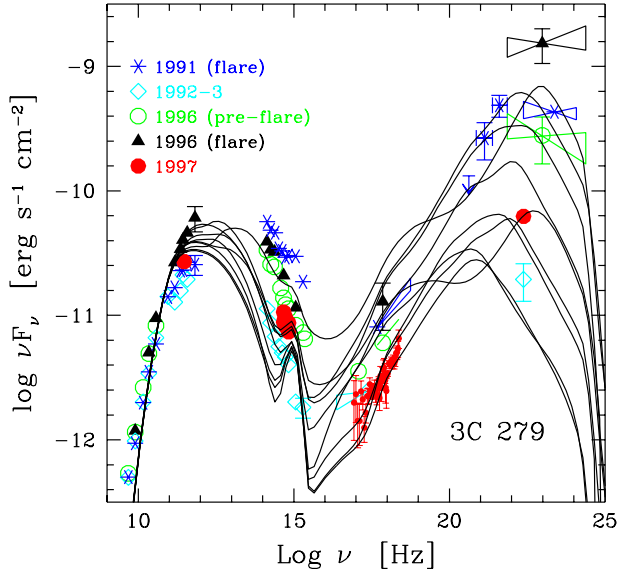


Figure 8. Example of the spectra predicted by our model compared with the SED of 3C 279 corresponding to different observational campaigns.

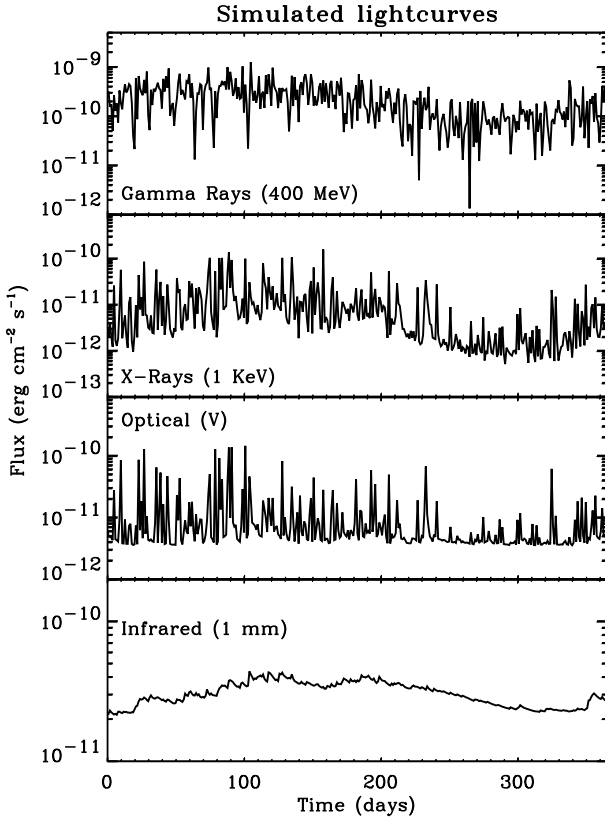


Figure 9. Light curves at different frequencies. The γ -rays, X-rays and Optical light curves vary on different time scale, with a minimum value of few hr, and the IR one varies on few months time scale.

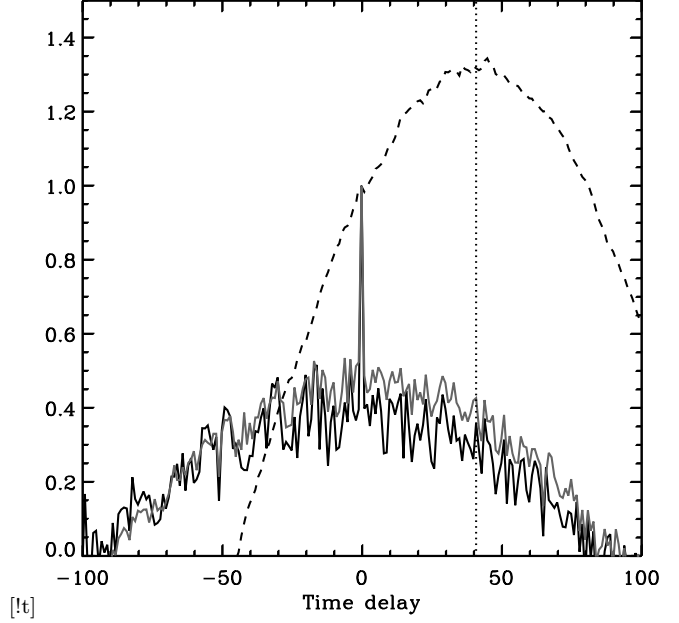


Figure 10. Results of cross correlations between γ -rays and X-ray (solid grey line), optical (solid dark line) and infrared (dashed line) light curves. The X-rays and optical emission vary simultaneously with the γ -rays, while the IR follows the γ -rays emission with a delay of a ~ 40 days (the vertical dotted line).

active regions is inside the BLR. The lower line shows the SED in a quiescent state of the source, i.e. when all of the active collisions are located outside the BLR. The difference between the two spectra manifests itself mainly in the high frequency range, where the internal collisions, that have a shorter pulse duration, mostly contribute. Although the number of external collisions is almost equal to the number of the inner ones, the former produce longer pulses: it follows that the number of those simultaneously active is higher and hence the statistical variability is suppressed.

A different way to examine the results is to determine light curves in given energy bands: Figure 9 shows the flux temporal behavior in the γ -ray, X-ray, optical and millimeter ranges. The high frequency fluxes (down to optical energies) are highly variable (again since they are produced mainly by the inner collisions), while the millimeter flux comes from outer shocks and thus the corresponding light curve is much smoother.

In order to study the presence of delays in the variability at different wavelengths, we added “secular” variations in the kinetic luminosity injected by the inner engine. In particular, this is modulated as a sinusoidal function with period ~ 1 year, spanning a factor of five in luminosity (between the minimum and the maximum). Figure 10 illustrates the results of the cross correlations between the γ -ray and the other frequencies light curves. Once again the plot shows that γ -ray, X-ray and optical photons are produced in the same region (being closely correlated, with no time delay), while the IR emission lags by ~ 40 days, as the shells that produce high frequency photons inside the BLR have to travel to larger radii ($R \sim 10^{19}$ cm) to produce IR emission. The expected observed delay is given by:

$$\Delta t = \frac{\Delta R}{c\Gamma^2} \sim 38.5 \Delta R_{19} \Gamma_1^{-2} \text{ days}, \quad (30)$$

which indeed well describes the results of the simulations.

Finally note that time delays of the order of \sim hr might occur between γ -ray and X-ray/optical peaks even if they are produced in the same region. However, the study of such delays would require to take into account the different light travel paths within a single region (Chiaberge & Ghisellini 1999), and a time dependent treatment of the shell emission, taking into account the variations in the magnetic field and electron distribution during the cooling. Such a treatment is beyond the scope of the present work and will be examined in future developments of the model.

6 DISCUSSION

Highly relativistic flows dominate the dynamics and emission in both Gamma-Ray Bursts and blazars. It has been proposed that internal shocks, produced by the interaction of flow components injected with different bulk speeds, can be responsible for the observed emission and variability in both classes of sources (Rees 1978; Rees & Meszaros 1994).

Here we have considered in some details this ‘internal shock’ scenario in the context of AGN jets, self-consistently accounting for the dynamics and the radiative properties of the flow. After describing the kinematic and radiative assumptions of the model, we have examined the results of numerical simulations which allow us to study the predicted energy deposition on different jet scales, the relevant timescales, the corresponding dominating emission processes, the spectral evolution and predicted variability, the correlations among the emission at different frequencies.

The key interesting features of this scenario are the relatively low radiative efficiency (of order of a few per cent) which well accounts for the dissipation of kinetic energy in blazars, as higher dissipation rates would create major energetic problems (in order to carry sufficient power up to the large scale lobe structures). Furthermore, although the radiative dissipation occurs on all jet scales, as indeed observed, the bulk of it is localized at tenths of a pc, on the BLR scale, in agreement with the requirements of fast variability and transparency to γ -rays.

The results of the simulations, based on input parameters suitable to qualitatively reproduce the observations of a powerful radio-loud quasar, such as 3C 279, are indeed satisfactory. As expected the plasma in the inner part of the jet cools predominantly via EC emission, while on larger scales synchrotron cooling dominates. Qualitative agreement is also obtained in terms of light curves, and correlations among different spectral bands are predicted. Also, an asymptotic value of the bulk Lorentz factor $\Gamma \sim 15$ is achieved at distances \sim pc.

While this paper has been aimed at presenting the model and study its general applicability to blazar jets, the final goal is to determine which initial parameters/conditions are required in order to produce the whole of the blazar phenomenology and energetics. In particular, the model significantly constrains the typical Lorentz factors (and their distribution) achieved through acceleration on the inner scales, and the typical timescale of plasma injection. In this respect, also the determination of the duty cycle of the γ -ray emission in blazars is of chief importance, as it can be used to constrain the rate and Lorentz factor

distribution of the injection of energy/plasma in the relativistic flow. Note that although more accurate measures of γ -ray spectra and the detection of a much larger number of γ -ray loud sources will require the capabilities of GLAST, tight constraints on the duty cycles will be available much sooner thanks to the launch of AGILE. The model presented here will provide (for the first time) the possibility of directly modelling the time dependent broad band spectral evolution of these sources following the (time dependent) energy injection. The relationship between flares at high energies and the birth of superluminal radio knots and/or radio flares will be also explored.

Therefore issues associated with the jet energy content and the relative conversion of bulk energy into internal (particle and field) energy at relativistic shocks can be also constrained by the comparison of the model predictions with observations.

A further aspect we intend to examine is the propagation and dissipation of jets on larger scales, where however uncertainties are large. On the \gg pc-scales, significant entrainment might occur, possibly leading to the formation of external shocks and the development of slower outer layers around jets. Another issue is the relative importance of creation vs amplification of an existing seed magnetic field: if the latter process prevails, it will probably lead to larger magnetic fields on the kpc scale jet, and consequently to faster synchrotron cooling. Inverse Compton cooling at kpc scales is instead enhanced, with respect to what calculated here, by the interaction of with the cosmic background radiation, which is seen relativistically boosted in the rest frame of the fast moving parts of the jets (e.g. Celotti, Ghisellini & Chiaberge, 2000).

We finally stress that it is of primary importance, for the understanding of the flow injection and its connection with the central accreting engine, to determine the key parameters which regulate the observed spectral and luminosity trend, from high power, low energy peaked, flat spectrum radio quasars, to weak high energy peaked BL Lacs (Fossati et al. 1998). This will be the content of a forthcoming paper.

7 ACKNOWLEDGMENTS

We wish to thank the anonymous referee for his/her constructive and careful comments. The Italian MURST is acknowledged for financial support (AC).

REFERENCES

- Bednarz J., Ostrowski M., 1998, Phys. Review Letters, 80, 3911
- Beloborodov A.M., 2000, ApJ, 539, L25
- Blandford R.D. & McKee C.F., 1976, Phys. of Fluids, 19, 1130
- Celotti A. & Fabian A.C., 1993, MNRAS, 264, 228
- Celotti A., Maraschi L. & Treves A., 1991, ApJ, 377, 403
- Celotti A., Ghisellini G. & Chiaberge M., 2000 MNRAS in press (astro-ph/0008021)
- Chiaberge M. & Ghisellini G., 1999, MNRAS, 306, 551
- Daigne F., Mochkovitch R. 1998, MNRAS, 296, 275
- Fossati G., Maraschi L., Celotti A., Comastri A. & Ghisellini G., 1998, MNRAS, 299, 433
- Ghisellini G. & Maraschi L., 1989, ApJ, 340, 181
- Ghisellini G., Svensson R., 1991, MNRAS, 252, 313.

- Ghisellini G., Padovani P., Celotti A. & Maraschi L., 1993, ApJ, 407, 65
- Ghisellini G., Madau P., 1996, MNRAS, 280, 67
- Ghisellini G., Celotti A., Fossati G., Maraschi L. & Comastri A., 1998, MNRAS, 301, 451
- Georganopoulos M. & Marscher A.P., 1998, ApJ, 506, L11
- Hartman R.C. et al. 1996, ApJ, 461, 698
- Inoue S. & Takahara F., 1996, ApJ, 463, 555
- Kirk J. G., Guthmann, A. W., Gallant, Y. A. & Achterberg, A., 2000, ApJ, 542, 235.
- Kobayashi S., Piran T. & Sari R. 1998, ApJ, 490, 92
- Lazzati D., Ghisellini G. & Celotti A., 1999, MNRAS, L13
- Maraschi L., Ghisellini G. & Celotti A., 1992, ApJ, 377, 403
- Maraschi L. et al., 1994, ApJ, 435, L91
- Panaitescu A. & Mészáros P., 1999, ApJ, 526, 707
- Panaitescu A., Spada M. & Mészáros P., 1999, ApJ, 522, L105
- Piran T., 1999, Physics Reports, 314, 575
- Rawlings S., Saunders R., 1991, Nature, 349, 138
- Rees M.J., 1978, MNRAS, 184, P61
- Rees M.J. & Mészáros P., 1994, ApJ, 430, L93
- Sikora M., Begelman M., Rees M.J., 1994, ApJ, 421,153
- Spada M., Panaitescu A. & Mészáros P., 2000, ApJ, 537, 824
- Ulrich M.-H., Maraschi L. & Urry C.M., 1997, ARA&A, 35, 445
- Wagner S.J. & Witzel A., 1995, ARA&A, 33,163
- Zensus J.A. et al., 1997, ARA&A, 35, 607